nature physics

LETTERS

https://doi.org/10.1038/s41567-019-0772-5

Buffer gas cooling of a trapped ion to the quantum regime

T. Feldker[1], H. Fürst[1], H. Hirzler[1], N. V. Ewald[1], M. Mazzanti[1], D. Wiater[2], M. Tomza[2] and R. Gerritsma[1*]

Great advances in precision measurements in the quantum regime have been achieved with trapped ions and atomic gases at the lowest possible temperatures[1–3]. These successes have inspired ideas to merge the two systems[4]. In this way, we can study the unique properties of ionic impurities inside a quantum fluid[5–12] or explore buffer gas cooling of a trapped-ion quantum computer[13]. Remarkably, in spite of its importance, experiments with atom–ion mixtures have remained firmly confined to the classical collision regime[14]. We report a collision energy of 1.15(±0.23) times the *s*-wave energy (or 9.9(±2.0) μK) for a trapped ytterbium ion in an ultracold lithium gas. We observed a deviation from classical Langevin theory by studying the spin-exchange dynamics, indicating quantum effects in the atom–ion collisions. Our results open up numerous opportunities, such as the exploration of atom–ion Feshbach resonances[15,16], in analogy to neutral systems[17].

Neutral buffer gas cooling of trapped ions has a long history[18], dating back to when laser cooling was still in its infancy. The development of atom trapping spurred efforts to employ quantum degenerate buffer gases. These are readily prepared in the 100 nK regime by evaporative cooling, making them superb coolants. Despite this, it is well known that the time-dependent electric potential of a Paul trap complicates matters[19]. It causes a fast-driven motion in the ions called micromotion, from which energy can be released when an ion collides with an atom. This leads to a situation in which the kinetic energy of the ion becomes much larger than that of the surrounding buffer gas. Because of this, buffer gas cooling remained uncompetitive compared with laser cooling of the ions. It has also prevented the study of interacting ions and atoms in the quantum regime, and reported collision energies of atom–ion mixtures have been at least two orders of magnitude higher than the *s*-wave energy[14]. It was suggested that this effect could be mitigated by employing an ion–atom combination with a large mass ratio[20], such as Yb^+ and ^6Li.

We trap and Doppler cool a single $^{171}Yb^+$ ion in a Paul trap (Fig. 1a). We prepare a cloud of 5×10^3 to 2×10^4 ^6Li atoms per spin state in a mixture of $|F=1/2, m_F=\pm1/2\rangle$, where F is the total angular momentum quantum number and m_F is its projection onto the quantization axis, and a temperature of $T_a=2$–$10\,\mu K$ in an optical dipole trap 50 μm below the trapped ion (see Methods). The atoms are transported up by repositioning the dipole trap using piezo-controlled mirrors. After a variable interaction time, the optical dipole trap is switched off, and the ion is interrogated with a spectroscopy laser pulse at 411 nm that couples the $S_{1/2}$ ground state to the long-lived $D_{5/2}$ state (Fig. 1b). We obtain the average kinetic energy of the ion by studying this laser excitation as a function of pulse width[8,21]. In particular, the Rabi frequency Ω of oscillations between the two states depends on the number of quanta n present in the motion of the ion in its trap. Thermal occupation of excited states results in mixing of frequency components and thus damping of the Rabi oscillation. We fit the observed excitation to a model that assumes a thermal distribution with $\bar{n}$ motional quanta on average (mean). From this, we obtain the ion's secular temperature in the radial direction $T^{\perp}_{sec} \propto \bar{n}$ (see Methods).

We observe buffer gas cooling of the ion by temperature measurements after various hold times of the trapped ion in the ultracold cloud. The result for an atomic cloud with $T_a=10\,\mu K$ and peak density $\rho=31(\pm15)\times10^{15}\,m^{-3}$ is shown in Fig. 2a. Initially, the ion has about $T^{\perp}_{sec}=600\,\mu K$, which is close to the Doppler cooling limit. Then, the ion cools down with a 1/e time of $\tau_{cool}=244(\pm24)$ ms to a final temperature of $T^{\perp}_{sec}=98(\pm11)\,\mu K$, corresponding to $\bar{n}=5.8(\pm0.7)$ in the radial directions of motion. The buffer gas cooling thus outperforms Doppler cooling by a factor of ~5 in terms of attained temperature.

Note that the final ion temperature in Fig. 2a is about an order of magnitude larger than the temperature of the buffer gas. This behaviour may be a direct consequence of the time dependence of the ionic trapping potential[8,22–26], which causes energy release from the ion's micromotion during a collision. We investigate this by comparing the observed dynamics of the ion in the buffer gas with classical molecular dynamics simulations[27], in which we draw the ion's initial secular energy from a Maxwell–Boltzmann distribution at $T_{sec}=609\,\mu K$ to match the data.

If we run the simulations assuming a static ion trapping potential for the ion (known as the secular approximation[28]), we find complete thermalization, $T_{sec}\rightarrow T_a$, as shown by the dotted line in Fig. 2a. We improve our model by including the time dependence of the Paul trap, using parameters obtained from our experiment, including all sources of micromotion (see Methods). In this simulation, a final ion temperature of 43 μK is reached. When we also include the background heating rate of $85(\pm50)\,\mu K\,s^{-1}$, which was measured in the absence of the atoms, the simulated final ion temperature reaches $63(\pm12)\,\mu K$, as shown by the dashed line in Fig. 2a. A likely explanation for the remaining discrepancy in the final temperature is overestimation of the ion's kinetic energy by neglecting other dephasing mechanisms in the Rabi oscillations, such as laser frequency noise. Quantum corrections may also play a role at the small energies we obtain[29]. Finally, spin relaxation of atoms during collisions[7,10,30] may also account for some background heating.

To reach even lower energies in the experiment, we cool the atoms to $T_a=2.3(\pm0.4)\,\mu K$ and adiabatically lower the radial trap frequency for the ion from $\omega_x\approx\omega_y=2\pi\times330\,kHz$ to $\omega_x\approx\omega_y=2\pi\times210\,kHz$

[1]Van der Waals-Zeeman Institute, Institute of Physics, University of Amsterdam, Amsterdam, The Netherlands. [2]Faculty of Physics, University of Warsaw, Warsaw, Poland. *e-mail: r.gerritsma@uva.nl

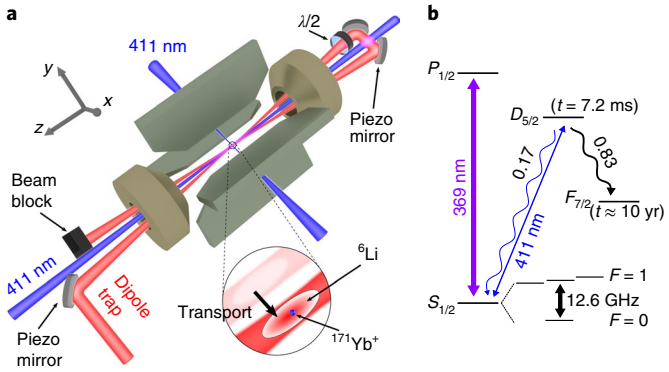

Fig. 1 | Set-up. a, A cloud of ultracold ^{6}Li atoms is prepared in an optical trap ~50 μm below a single ion in a Paul trap (shown in grey). The optical trap is operated in crossed-beam configuration; a $\lambda/2$ waveplate turns the polarization of the second beam by 90° in order to avoid the formation of an optical lattice. The ion is then immersed in the atomic cloud by transporting the atom trap up using piezo-controlled mirrors. **b**, The ions are Doppler-cooled on the 369-nm $S_{1/2}\rightarrow P_{1/2}$ transition. After a variable atom–ion interaction time, the ion is interrogated by coupling the $S_{1/2}$ ground state on a narrow quadrupole transition to the $D_{5/2}$ excited state. The coupling strength of the transition can be directly related to the temperature of the ion. The $D_{5/2}$ state decays with probabilities of 0.83 to the $F_{7/2}$ state (lifetime $t \approx 10$ years) and 0.17 to the $S_{1/2}$ state. State-selective fluorescence detection allows us to establish the average coupling strength. A microwave at 12.6 GHz couples the hyperfine states $F = 1$ and $F = 0$ of the $S_{1/2}$ ground state.

at the end of 1 s of buffer gas cooling. In this way, we achieve $T^{\perp}_{\rm sec}=42(\pm19)$ μK, corresponding to $\bar{n}=3.7(\pm1.4)$ (Fig. 2b).

The total kinetic energy of the ion can be written as $E_{\rm i}=E_{\rm sec}+E_{\rm iMM}+E_{\rm eMM}$, that is, the secular energy plus the energy due to the intrinsic (iMM) and excess micromotion (eMM). To obtain the total collision energy, we must additionally determine the axial secular temperature, $T^{\rm ax}_{\rm sec}$, and the various micromotion energies.

Owing to the weak confinement along the trap axis ($\omega_z=2\pi\times130$ kHz), it is more convenient to probe the excitation probability as a function of the frequency of the laser, which we now direct along the z axis. Thermal motion leads to Doppler broadening of the resonance (Fig. 2c). We fit a Gaussian distribution to the data and find the standard deviation $\sigma=193(\pm26)$ kHz, corresponding to $T^{\rm ax}_{\rm sec}=130(\pm35)$ μK. There are two reasons for the larger value compared with $T^{\perp}_{\rm sec}$: first, the weaker axial trap potential gives rise to a higher background heating rate (200 μK s^{-1}) and thus limits the attainable final temperature; second, the thermometry method is less reliable and more prone to overestimation of the temperature due to saturation broadening.

Intrinsic micromotion leads to a kinetic energy of $E_{\rm iMM}\approx k_{\rm B}T^{\perp}_{\rm sec}$ (ref. [28]), where $k_{\rm B}$ is Boltzmann's constant. Excess micromotion occurs because of experimental imperfections that modify the trap potential. Details of the compensation and characterization of excess micromotion can be found in Methods. In the experiment, we find $E_{\rm eMM}/k_{\rm B}\leq44(\pm13)$ μK.

The collision energy is given by[27]

$$E_{\rm col}=\frac{\mu}{m_{\rm i}}E_{\rm i}+\frac{\mu}{m_{\rm a}}E_{\rm a} \qquad (1)$$

with $m_{\rm i}$ and $m_{\rm a}$ the mass of the ion and atom, respectively, μ the reduced mass and $E_{\rm a}=3k_{\rm B}T_{\rm a}/2$ the average kinetic energy of the atoms. Note that, owing to the large mass ratio, $\mu\approx m_{\rm a}\ll m_{\rm i}$. Taking into account the contribution of all types of motion (Table 1) results in a collision energy of $E_{\rm col}=1.15(\pm0.23)\times E_s$, with $E_s/k_{\rm B}=8.6$ μK the s-wave collision energy[4].

Since we cooled the mixture close to the s-wave limit, we expect signatures of quantized angular momentum to occur in the collisions. To look for signs of quantum effects in the interaction,

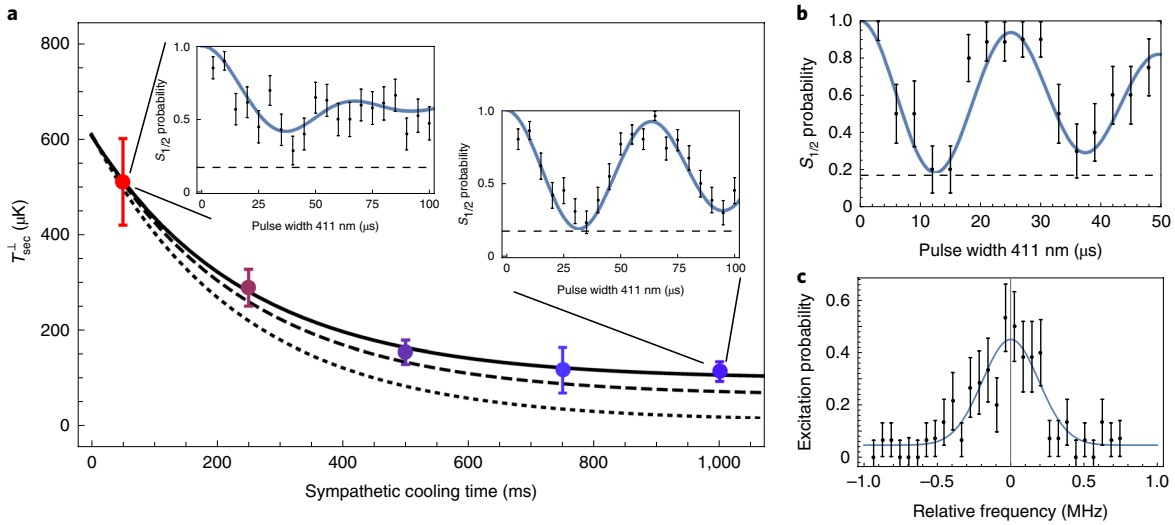

Fig. 2 | Cooling dynamics of an ion in the ultracold buffer gas. a, Ion temperature as a function of atom–ion interaction time, together with an exponential fit (solid line) and molecular dynamics simulations with and without taking into account the time dependence of the Paul trap (dashed and dotted lines, respectively). Before buffer gas cooling, the temperature of the ion is close to the Doppler laser cooling limit. This results in a rapidly decaying Rabi oscillation as a function of laser interrogation pulse width (inset). After buffer gas cooling, the Rabi oscillations persist for much longer. The branching ratio of decay out of the $D_{5/2}$ state limits the contrast of the Rabi oscillations to 0.83, as indicated by the dashed horizontal lines. The blue lines in the insets show the least-squares fit lines, from which we attain the ion temperature. **b**,**c**, Measurement of radial ($T^{\perp}_{\rm sec}=42(\pm19)$ μK) (**b**) and axial ($T^{\rm ax}_{\rm sec}=130(\pm35)$ μK) (**c**) temperatures after 1 s of interaction time with an atomic cloud with $T_{\rm a}=2.3(\pm0.4)$ μK and after adiabatic decompression of the radial ion trap potential. The blue lines show the least-squares fit lines; the dashed line in **b** indicates the attainable contrast limited by the branching ratio. Error bars for the state detection denote the quantum projection noise, while error bars for temperatures denote the standard deviation obtained from the fits.

Table 1 | Measured energy budget of the trapped ion and atoms in terms of kinetic energy (E_{kin}) and collision energy

Type of motion	E_{kin}/k_B (μK)	E_{col}/k_B (μK)
Radial secular ion	2 × 21(±9)	1.4(±0.6)
Intrinsic micromotion	2 × 21(±9)	1.4(±0.6)
Axial secular ion	65(±18)	2.2(±0.4)
Excess micromotion	44(±13)	1.5(±0.4)
Total ion energy	**193(±42)**	**6.6(±1.4)**
Atom temperature	3/2 × 2.3(±0.4)	3.3(±0.6)
Total collision energy	—	**9.9(±2.0)**

The atomic energy is obtained from time-of-flight analysis after the 1-s buffer gas cooling time. Errors are given in microkelvin.

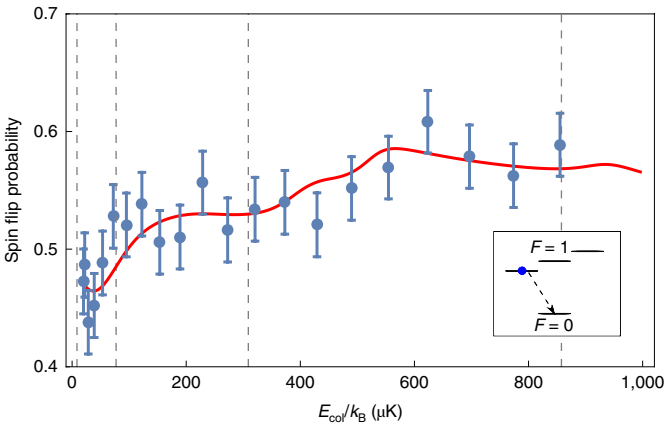

Fig. 3 | Spin-exchange rate versus collision energy. Probability of detecting the ion spin in $|F=0, m_F=0\rangle$ after preparing it in $|F=1, m_F=-1\rangle$ and letting it interact with the atomic cloud for ~10 ms. The collision energy is varied using an offset field to tune the excess micromotion energy. The red solid line is obtained by convolving the rate from quantum scattering calculations with the energy distribution of the ion (see Methods). Both theory and data show a clear deviation from classical behaviour in which the spin-exchange rate should be independent of collision energy. The dashed vertical lines indicate the heights of the energy barriers for the first four collisional angular momentum states $l=1,\ldots,4$. The inset shows the measured spin-exchange process in the ion (blue dot). Error bars denote the quantum projection noise.

we investigate the occurrence of spin-changing collisions[7,10,30] as a function of collision energy. Spin exchange is associated with short-range collisions between the atoms and ions, known as Langevin collisions. In the classical regime, the Langevin collision rate is strictly independent of collision energy[4]. At very low collision energy, however, quantization of the collision angular momentum and quantum reflection start to play a role. This leads to the occurrence of structure such as shape resonances in the spin-exchange rate. The details of this structure depend on the singlet and triplet scattering lengths that quantify the interactions between the atom and ion in the quantum regime.

After buffer gas cooling for 1 s in an atomic cloud with $T_a = 11.6(\pm 0.5)\,\mu\mathrm{K}$, we prepare the ion in the state $|S_{1/2}, F=1, m_F=-1\rangle$, with a microwave pulse. The atomic ensemble is in a spin mixture of the lowest two Zeeman states $|S_{1/2}, F=1/2, m_F=\pm 1/2\rangle$. Due to spin-exchange collisions during the interaction time, the ion can relax to the $|S_{1/2}, F=0, m_F=0\rangle$ state. We let the ion interact with the cloud of atoms with a density of $21(\pm 10)\times 10^{15}\,\mathrm{m}^{-3}$ for ~10 ms, corresponding to about one Langevin collision. Only during the interaction time, we give the ion a variable amount of excess micromotion energy by ramping offset voltages on compensation electrodes[4]. We then shelve the population that remains in the $|S_{1/2}, F=1\rangle$ state to the long-lived $F_{7/2}$ state. Subsequent fluorescence detection allows us to discriminate between an ion in the $|S_{1/2}, F=0\rangle$ state (spin exchange) and an ion in the $F_{7/2}$ state (no spin exchange) with near unit fidelity. Figure 3 shows the result of averaging 309 such experimental runs. We see a notable dependence of the spin-exchange rate on the collision energy and thus a clear deviation from the classical prediction, particularly for low collision energies.

To gain further insight, we compare the data with multichannel quantum scattering calculations based on the complete description of molecular and hyperfine structures. The amplitude, slope and shape of the rate constants in the investigated energy range depend strongly on the values of the singlet and triplet scattering lengths. Figure 3 presents the calculated rate constants for the spin-exchange collisions convoluted with the experimental collision energy distribution for the singlet and triplet scattering lengths of $a_S = 1.2R_4$ and $a_T = -1.5R_4$, with $R_4 = 70\,\mathrm{nm}$ (ref. [4]), and 1.2 Langevin collisions on average during the interaction time. These values provide the best fit to the experimental data (see Methods).

In conclusion, we have demonstrated buffer gas cooling of a single ion in a Paul trap to the quantum regime of atom–ion collisions. This has been an elusive goal in hybrid atom–ion experiments for more than a decade[4]. The data and simulations suggest that even lower temperatures may be reached when using colder and denser atomic clouds, both of which are technically feasible. In particular, a denser cloud would allow elimination of the background heating rate of the ion. We speculate that controlling elastic atom–ion collisions using possible Feshbach resonances[15,16] may allow the cooling rate and accessible temperatures in atom–ion mixtures to be tuned further, as is the case in neutral systems[17].

Online content

Any methods, additional references, Nature Research reporting summaries, source data, extended data, supplementary information, acknowledgements, peer review information; details of author contributions and competing interests; and statements of data and code availability are available at https://doi.org/10.1038/s41567-019-0772-5.

Received: 11 July 2019; Accepted: 6 December 2019;
Published online: 3 February 2020

References

1. Ludlow, A. D., Boyd, M. M., Ye, J., Peik, E. & Schmidt, P. Optical atomic clocks. *Rev. Mod. Phys.* **87**, 637–701 (2015).
2. Bernien, H. et al. Probing many-body dynamics on a 51-atom quantum simulator. *Nature* **551**, 579–584 (2017).
3. Zhang, J. et al. Observation of a many-body dynamical phase transition with a 53-qubit quantum simulator. *Nature* **551**, 601–604 (2017).
4. Tomza, M. et al. Cold hybrid ion–atom systems. *Rev. Mod. Phys.* **91**, 035001 (2019).
5. Zipkes, C., Paltzer, S., Sias, C. & Köhl, M. A trapped ion inside a Bose–Einstein condensate. *Nature* **464**, 388–391 (2010).
6. Schmid, S., Härter, A. & Denschlag, J. H. Dynamics of a cold trapped ion in a Bose–Einstein condensate. *Phys. Rev. Lett.* **105**, 133202 (2010).
7. Ratschbacher, L. et al. Dynamics and decoherence of a single spin-qubit in a tunable environment. *Phys. Rev. Lett.* **110**, 160402 (2013).
8. Meir, Z. et al. Dynamics of a ground-state cooled ion colliding with ultra-cold atoms. *Phys. Rev. Lett.* **117**, 243401 (2016).
9. Kleinbach, K. S. et al. Ionic impurity in a Bose–Einstein condensate at submicrokelvin temperatures. *Phys. Rev. Lett.* **120**, 193401 (2018).
10. Sikorsky, T., Meir, Z., Ben-shlomi, R., Akerman, N. & Ozeri, R. Spin-controlled atom–ion chemistry. *Nat. Commun.* **9**, 920 (2018).
11. Haze, S., Sasakawa, M., Saito, R., Nakai, R. & Mukaiyama, T. Cooling dynamics of a single trapped ion via elastic collisions with small-mass atoms. *Phys. Rev. Lett.* **120**, 043401 (2018).

12. Schmidt, J., Weckesser, P., Thielemann, F., Schaetz, T. & Karpa, L. Optical traps for sympathetic cooling of ions with ultracold neutral atoms. Preprint at https://arxiv.org/abs/1909.08352 (2019).
13. Daley, A. J., Fedichev, P. O. & Zoller, P. Single-atom cooling by superfluid immersion: a nondestructive method for qubits. *Phys. Rev. A* **69**, 022306 (2004).
14. Schmid, T. et al. Rydberg molecules for ion–atom scattering in the ultracold regime. *Phys. Rev. Lett.* **120**, 153401 (2018).
15. Idziaszek, Z., Simoni, A., Calarco, T. & Julienne, P. S. Multichannel quantum-defect theory for ultracold atom–ion collisions. *New J. Phys.* **13**, 083005 (2011).
16. Tomza, M., Koch, C. P. & Moszynski, R. Cold interactions between an Yb^+ ion and a Li atom: prospects for sympathetic cooling, radiative association, and Feshbach resonances. *Phys. Rev. A* **91**, 042706 (2015).
17. Chin, C., Grimm, R., Julienne, P. S. & Tiesinga, E. Feshbach resonances in ultracold gases. *Rev. Mod. Phys.* **82**, 1225–1286 (2010).
18. Itano, W. M., Bergquist, J. C., Bollinger, J. J. & Wineland, D. J. Cooling methods in ion traps. *Phys. Scr.* **1995**, 106–120 (1995).
19. Major, F. G. & Dehmelt, H. G. Exchange-collision technique for the RF spectroscopy of stored ions. *Phys. Rev.* **170**, 91–107 (1968).
20. Cetina, M., Grier, A. T. & Vuletić, V. Fundamental limit to atom–ion sympathetic cooling in Paul traps. *Phys. Rev. Lett.* **109**, 253201 (2012).
21. Leibfried, D. et al. Experimental determination of the motional quantum state of a trapped atom. *Phys. Rev. Lett.* **77**, 4281–4285 (1996).
22. DeVoe, R. G. Power-law distributions for a trapped ion interacting with a classical buffer gas. *Phys. Rev. Lett.* **102**, 063001 (2009).
23. Zipkes, C., Ratschbacher, L., Sias, C. & Köhl, M. Kinetics of a single trapped ion in an ultracold buffer gas. *New J. Phys.* **13**, 053020 (2011).
24. Chen, K., Sullivan, S. T. & Hudson, E. R. Neutral gas sympathetic cooling of an ion in a Paul trap. *Phys. Rev. Lett.* **112**, 143009 (2014).
25. Rouse, I. & Willitsch, S. Superstatistical energy distributions of an ion in an ultracold buffer gas. *Phys. Rev. Lett.* **118**, 143401 (2017).
26. Höltkemeier, B., Weckesser, P., López-Carrera, H. & Weidemüller, M. Buffer-gas cooling of ions in a multipole radio frequency trap beyond the critical mass ratio. *Phys. Rev. Lett.* **116**, 233003 (2016).
27. Fürst, H. et al. Prospects of reaching the quantum regime in Li–Yb^+ mixtures. *J. Phys. B* **51**, 195001 (2018).
28. Berkeland, D. J., Miller, J. D., Bergquist, J. C., Itano, W. M. & Wineland, D. J. Minimization of ion micromotion in a Paul trap. *J. Appl. Phys.* **83**, 5025–5033 (1998).
29. Krych, M. & Idziaszek, Z. Description of ion motion in a Paul trap immersed in a cold atomic gas. *Phys. Rev. A* **91**, 023430 (2015).
30. Fürst, H. et al. Dynamics of a single ion-spin impurity in a spin-polarized atomic bath. *Phys. Rev. A* **98**, 012713 (2018).

Methods

Preparation of atomic clouds. The cloud of ^{6}Li atoms is prepared by loading a crossed optical dipole trap from a magneto-optical trap close to the trapped ion. The crossed dipole trap is formed by a fibre laser at 1,064 nm with a maximum output power of 200 W. By operating the laser in lin⊥lin polarization configuration, where the two beams forming the crossed dipole trap have perpendicular polarization, we prevent the occurrence of an optical lattice potential. At the end of the loading stage, we optically pump the ^{6}Li atoms into a 50/50 mixture of the lowest two spin states, $|F=1/2, m_F=\pm 1/2\rangle$. We increase the magnetic field to ~ 66.3 mT to increase the collision rate between the atoms, and evaporate down to 10 μK in 1.5 s by lowering the power of the dipole trap laser. After evaporation, the magnetic field is reduced to 0.4 mT, such that the atoms cease to interact strongly, and the cloud is transported up to the trapped ion (see main text). Overlap with the ion is assured by measuring the Stark shift caused by the dipole trap on the trapped ion, and by optimizing charge transfer collisions when preparing the ion in the metastable $D_{3/2}$ state[31]. For the experiments with atoms at 2.3 μK, we first evaporate down to 15 μK, after which, we switch the magnetic field to 30 mT. Since the scattering length between the two spin states is negative at this field, we prevent the creation of Li_2 halo dimers at ultralow temperatures in this way[17]. These would complicate the interpretation of our results.

The atom number and temperature are monitored by time-of-flight analysis in combination with spin-selective absorption imaging. We image the cloud through holes in the endcaps of the Paul trap, that is, along the z direction. Time-of-flight data for expansion in the x and y directions are shown in Extended Data Fig. 1, both for the initial cloud ($T_a = 2.6(\pm 0.3)$ μK, 9×10^3 atoms per spin state) and after the 1 s buffer gas cooling time ($T_a = 2.0(\pm 0.8)$ μK, 5.5×10^3 atoms per spin state). We do not observe a substantial change in atom temperature after interaction with the ion. Since the temperature after the buffer gas cooling is slightly colder, but less accurate, compared with the temperature before buffer gas cooling, we chose to give the average of the two temperatures in the energy budget. The atom loss is comparable to the atom loss when there is no ion present. Further details of the preparation and analysis of the trapped atoms can be found in refs. [30–33]. The time-of-flight data for the atomic cloud used in the spin-exchange experiments are shown in Extended Data Fig. 1c ($T_a = 11.6(\pm 0.5)$ μK, 20×10^3 atoms per spin state). From the data, we extract atomic trap frequencies of $2\pi\times(490(\pm 70), 470(\pm 140))$ Hz in the radial directions for the coldest atomic clouds. Based on the aspect ratio of the atomic cloud[32], the axial trap frequencies are a factor of ~10 smaller still. Since these values are negligible compared with the trap frequencies of the ion, the atoms can be treated as free particles in our simulations and in the interpretation of our data.

Determination of ion energy. To obtain information on its motional state, the ion is interrogated with a spectroscopy laser pulse at 411 nm that couples the $|S_{1/2}, F=0, m_F=0\rangle$ state to the $|D_{5/2}, F'=2, m_F'=0\rangle$ state (Fig. 1). This state will decay to the long-lived $F_{7/2}$ state or back to the ground state with probabilities of 0.83 and 0.17, respectively[34]. Subsequent fluorescence imaging allows us to detect these states with near unit fidelity. The Rabi frequency of oscillations on the spectroscopy transition depends on the amount of motional quanta n_i present in the secular motion of the ion according to $\Omega = \Omega_0 \prod_{i=x,y,z} e^{-\eta_i/2} L_{n_i}(\eta_i^2)$ (refs. [8,21]), where Ω_0 is the ground-state Rabi frequency, $\eta_i = k_i l^{ho}$ is the Lamb–Dicke parameter, k_i is the wave vector of the 411 nm light projected onto the direction of ion motion i, $l^{ho} = \sqrt{\hbar/(2m_i\omega_i)}$ is the size of the ionic ground-state harmonic oscillator (ho) wave packet for a trap frequency ω_i, $L_{n_i}(\eta_i^2)$ is the Laguerre polynomial and $\hbar$ is Planck's constant/2π. Since the laser beam has a 45° angle with respect to the x and y directions of ion motion and $\omega_x \approx \omega_y = \omega_{rad}$, we set $\eta_x = \eta_y = \eta/\sqrt{2}$ and $\eta_z = 0$ for the measurements of the radial motion. Thermal occupation of excited states results in mixing of frequency components and thus damping of the Rabi oscillation. To obtain the ion temperature $T_{sec}^{\perp} = \hbar\omega(\bar{n}+1/2)/k_B$ with $\bar{n} = (\bar{n}_x + \bar{n}_y)/2$, we fit the observed excitation to a model that assumes a thermal distribution with probability distribution $P_{n_{x,y}}(n) = \bar{n}_{x,y}^n/(1+\bar{n}_{x,y})^{n+1}$ for each direction of motion x and y. Here, we assume $\bar{n}_x = \bar{n}_y$.

Micromotion compensation. The Paul trap operates at a drive frequency of $\Omega_{RF} = 2\pi\times 1.85$ MHz, where 'RF' means radio frequency. The motion of an ion in the trap is composed of a secular part with eigenfrequencies $\omega_x, \omega_y, \omega_z$ and its intrinsic and excess micromotion at Ω_{RF}. Intrinsic micromotion cannot be avoided and leads to an additional kinetic energy of the order of $E_{iMM} \approx k_B T_{sec}^{\perp}$ (ref. [28]). Buffer gas cooling to ultracold temperatures requires excellent control over excess micromotion. Not only does excess micromotion hinder cooling to the lowest secular temperatures as energy from the fast-driven micromotion can be transferred to the secular motion of the ion during a collision with an ultracold atom, but the kinetic energy stored in the micromotion increases the overall collision energy. In the following, we describe our methods to compensate micromotion to the required level. Furthermore, we give a detailed analysis of the micromotion energy budget.

Stray fields. The primary cause of excess micromotion is stray electric fields shifting the ion out of the RF-quadrupole node. We determine the remaining stray electric fields and the resulting excess micromotion with a set of two complementary methods. In the horizontal direction, we obtain the d.c. electric field by measuring the ion's position, by fluorescence imaging using a camera, as a function of radial trapping potential ω_{rad}. The position shift of the ion in an electric field $E_{d.c.}$ is given by

$$x(\omega_{rad}) = E_{d.c.} \times \frac{e}{m_{Yb}} \times \omega_{rad}^{-2} \quad (2)$$

where e denotes the elementary charge and m_{Yb} is the mass of the Yb^+ ion. Fitting the data, we obtain a stray field of $E_{d.c.} = 10(\pm 10)$ mV m^{-1}. To account for drifts between micromotion compensation measurements, we assume a slightly higher limit of $E_{d.c.} \leq 50$ mV m^{-1}. The average micromotion energy $\bar{E}_{eMM}$ is calculated as

$$\bar{E}_{eMM}(E_{d.c.}) = \frac{E_{d.c.}^2 \times e^2}{2m_{Yb} \times \omega_{rad}^2} \quad (3)$$

resulting in an excess micromotion energy of $\bar{E}_{eMM}/k_B \leq 4.7$ μK ($\bar{E}_{eMM}/k_B \leq 1.9$ μK) for a radial potential of $\omega_{rad} = 2\pi\times 210$ kHz ($\omega_{rad} = 2\pi\times 330$ kHz).

In the vertical direction, we measure stray fields using microwave Ramsey spectroscopy on the $(^2S_{1/2}, F=0) \leftrightarrow (^2S_{1/2}, F=1, m_F=1)$ transition. We apply a magnetic field gradient of $g_y = 0.17$ T m^{-1}, leading to a frequency shift of 2.3 kHz μm^{-1} in the transition. We determine the ion shift for $\omega_{rad} = 2\pi\times 25$ kHz and $\omega_{rad} = 2\pi\times 330$ kHz. From a linear fit to the measured frequency shifts, we obtain the required compensation voltage V_{comp}, with an uncertainty of 0.05 V. To account for daily drifts, we assume a miscompensation of $V_{comp} \leq 0.2$ V. We obtain the micromotion energy due to this miscompensation by calibrating the energy scale with resolved sideband spectroscopy on the narrow $^2S_{1/2} \leftrightarrow ^2D_{5/2}$ transition, as explained below. For $\omega_{rad} = 2\pi\times 210$ kHz, we obtain $\bar{E}_{eMM}/k_B \leq 8.3$ μK.

Energy calibration. We calibrate the excess micromotion energy versus voltage on the compensation electrodes by using resolved sideband spectroscopy on the $^2S_{1/2} \leftrightarrow ^2D_{5/2}$ transition. We use the magnetic field insensitive $(F=0, m_F=0) \leftrightarrow (F=2, m_F=0)$ transition in $^{171}Yb^+$. We compare the Rabi frequency on the micromotion sideband (Ω_{MM}) and on the carrier (Ω_{car}) at $V_{comp} = 7$ V, at a trap frequency of $\omega_{rad} = 2\pi\times 330$ kHz. We obtain $\Omega_{MM} = 2\pi\times 28.3(\pm 0.9)$ kHz and $\Omega_{car} = 2\pi\times 39.0(\pm 1.2)$ kHz. Solving

$$\frac{J_0(\beta_{MM})}{J_1(\beta_{MM})} = \frac{\Omega_{car}}{\Omega_{MM}} \quad (4)$$

with J_i denoting Bessel functions, yields a modulation index $\beta_{MM} = 1.18$. From the modulation index, we obtain the average kinetic energy as

$$\bar{E}_{eMM} = \frac{m}{4}\left(\frac{\beta_{MM}\times\Omega_{RF}}{k}\right)^2 \quad (5)$$

where k is the projection of the wave vector in the direction of the micromotion and $\Omega_{RF} = 1.85$ MHz. This results in $\bar{E}_{eMM}/k_B = 84(\pm 7)$ μK V$^{-2}\times V_{comp}^2$ and $\bar{E}_{eMM}/k_B = 208(\pm 19)$ μK V$^{-2}\times V_{comp}^2$ for $\omega_{rad} = 2\pi\times 330$ kHz and $\omega_{rad} = 2\pi\times 210$ kHz, respectively.

Quadrature micromotion. After carefully compensating any stray electric fields, we measure the remaining micromotion by resolved sideband spectroscopy. We set $\omega_{rad} = 2\pi\times 330$ kHz. We compare $\Omega_{car} = 2\pi\times 32.0(\pm 0.8)$ kHz at a laser power of $P = 32$ μW with $\Omega_{MM} = 2\pi\times 7.0(\pm 0.5)$ kHz at $P = 840$ μW. We obtain a micromotion energy of $\bar{E}_{eMM}/k_B = 21.5(\pm 1.5)$ μK. This value includes radial micromotion caused by remaining stray electric fields as well as quadrature micromotion caused by a phase difference of the RF signal on the opposing RF electrodes. Since we cannot differentiate between these types of radial micromotion, the obtained value is an upper limit for quadrature micromotion. The laser beam propagates at an angle of π/4 with respect to the direction of quadrature micromotion, so that we have to multiply the measured value by 2 to account for the full micromotion energy. Quadrature micromotion energy is proportional to the square of the trap frequency, so that we obtain $\bar{E}_{eMM}/k_B = 2\times 8.7(\pm 0.6)$ μK for $\omega_{rad} = 2\pi\times 210$ kHz.

Axial micromotion. Finite size effects of the linear Paul trap lead to a weak RF potential in the direction of the trap axis. Thus, the oscillating electric field vanishes at one point on the axis only. We position the single ion in our trap to this point and measure an upper limit to the remaining axial micromotion. Axial micromotion can, in principle, be measured in the same way as described for the quadrature micromotion, using a laser beam propagating along the trap axis. However, since our axial potential is weak, $\omega_{ax} \leq 2\pi\times 130$ kHz, and the corresponding Lamb–Dicke parameter $\eta_{ax} \geq 0.23$, we do not observe coherent oscillation when exciting with a laser beam propagating along the trap axis. To still measure an upper limit for axial micromotion, we compare a frequency scan over the carrier at very low power, $P = 61$ μW, with a scan over the micromotion sideband at full power, $P = 21.7$ mW. From Extended Data Fig. 2, we see that the transition on the micromotion sideband at these settings is not stronger than the

Table 2 | Measured excess micromotion budget of the trapped ion

Type of micromotion	$\bar{E}_{eMM}(210\,kHz)/k_B$ (μK)	$\bar{E}_{eMM}(330\,kHz)/k_B$ (μK)
Axial	13(±13)	33(±33)
Radial quadrature	2×8.7(±0.6)	2×21.5(±1.5)
Radial field (vertical)	≤8.3	≤3.4
Radial field (horizontal)	≤4.7	≤1.9
Total	44(±13)	82(±33)

Shown are the results for $\omega_{rad}=2\pi\times210$ kHz and $\omega_{rad}=2\pi\times330$ kHz. The total excess micromotion energy obtained at $\omega_{rad}=2\pi\times210$ kHz is $\bar{E}_{eMM}/k_B=44(\pm13)$ μK. Errors are given in microkelvin. The error is dominated by the error of the axial micromotion measurement.

carrier transition. From the ratio of laser powers, we calculate an upper bound to the axial micromotion of $\bar{E}_{eMM}/k_B=33$ μK for $\omega_{rad}=2\pi\times330$ kHz. If we reduce the radial trap potential to $2\pi\times210$ kHz, we obtain $\bar{E}_{eMM}/k_B=13$ μK. The limits obtained for micromotion energy at $\omega_{rad}=2\pi\times210$ kHz and $\omega_{rad}=2\pi\times330$ kHz are summarized in Table 2.

Tuning the collision energy. In the experiment, we tune the kinetic energy of the ion by shifting it out of the Paul trap centre with an electric control field $E_{d.c.}$. The resulting micromotion experienced by the ion causes a coherent motion with an energy distribution for $E\leq2\bar{E}_{eMM}(E_{d.c.})$:

$$P_{\bar{E}_{eMM}}(E)=\frac{1}{\pi}\frac{1}{\sqrt{E(2\bar{E}_{eMM}(E_{d.c.})-E)}} \quad (6)$$

To compare the data with the quantum scattering calculations, we convolute the calculated spin-exchange rates $\gamma(E)$ with this energy distribution. Here, we assume a thermal offset of 20 μK and use the maximum of the distribution to label the collision energy in Fig. 3.

Molecular dynamics simulations. We numerically simulate the full trapped-ion–atom system including the excess micromotion detected in our experiment. To model collisions, we introduce atoms one after another at a random location on a sphere of radius $r_0=0.6$ μm around a single ion. Each atom starts with a velocity drawn from a Maxwell–Boltzmann distribution at $T_a=10$ μK and passes the sphere, where it can interact with the ion. We set the interaction between the atom and ion to[27]

$$V_{ia}(r)=C_4\left(-\frac{1}{2r^4}+\frac{C_6}{r^6}\right) \quad (7)$$

with atom–ion distance $\boldsymbol{r}$, where $C_4=5.607\,J\,m^4$ for $^6Li/^{171}Yb^+$, and we set $C_6=5\times10^{-19}\,m^2$ to account for the short-range repulsion between the atom and ion. When the atom leaves the sphere, the ion's kinetic energy (averaged over the micromotion period) is obtained, and the next atom is introduced. We obtain the average ion cooling curve by averaging 300 simulation runs, containing $N_{at}=8{,}000$ atoms each.

We fit an exponential of the form $T^{\perp}_{sec}(n_{col})=(T_0-T_\infty)e^{-n_{col}/N_{eq}}+T_\infty$ to the simulated cooling dynamics. Here, n_{col} denotes the number of collsions while T_0 denotes the starting ion temperature before any atom-ion interactions. From this, we obtain the characteristic 1/e number of collisions N_{eq} it takes to equilibrate and the final ion temperature T_∞. From the average atomic flux $\phi_{at}=N_{at}/t_{prop}$ through the sphere within the total propagation time t_{prop}, we can translate N_{eq} into the 1/e number of Langevin collisions $N_{L,eq}$ via

$$N_{L,eq}=2\pi\rho_{sim}\sqrt{\frac{C_4}{\mu}}\frac{N_{eq}}{\phi_{at}} \quad (8)$$

Here, $\rho_{sim}=1/(4/3\pi r_0^3)$ is the atomic density in the simulation. By comparing with the experimental 1/e cooling time $\tau_{exp}=244(\pm24)$ ms, we can deduce the atomic density ρ_{at} in the experiment via the Langevin rate

$$\Gamma_L=\frac{N_{L,eq}}{\tau_{exp}}=2\pi\rho_{at}\sqrt{\frac{C_4}{\mu}} \quad (9)$$

to be $\rho_{at}=24(\pm3)\times10^{15}\ m^{-3}$, which is in agreement with the results from absorption imaging.

In the experiment, the buffer gas cooling is competing with ion heating caused by electric field noise. Independent measurements give a heating rate of $\gamma_{heat}=83(\pm50)\,\mu K\,s^{-1}$ in the radial direction in the absence of atoms. We account for this heating by setting $dT^{\perp}_{sec}(t)/dt=-\gamma_{cool}T^{\perp}_{sec}(t)+T_\infty\gamma_{cool}+\gamma_{heat}$, which results in $T^{\perp}_{sec}(t)=(T_0-T_\infty)e^{-\gamma_{cool}t}+T_\infty+\gamma_{heat}/\gamma_{cool}$, with $\gamma_{heat}/\gamma_{cool}\approx20$ μK and γ_{cool} the buffer gas cooling rate.

Finally, we obtain the energy distribution of secular ion motion from the numerical simulations. It has been found[8,22–26] that the energy distribution of a trapped ion can deviate substantially from a thermal distribution when interacting with a buffer gas. In our calculations, we do not find an observable difference from a thermal distribution for the secular motion of the ion after buffer gas cooling, as shown in Extended Data Fig. 3. We attribute this result to the large mass ratio between the atoms and ion[8,25].

Quantum scattering calculations. We construct and solve a quantum microscopic model of cold atom–ion interactions and collisions on the basis of the ab initio multichannel description of the Yb^+–Li system as presented in refs. [16,31]. The Hamiltonian used for the nuclear motion accounts completely for all relevant degrees of freedom, including the singlet and triplet molecular electronic states, the molecular rotation and the hyperfine and Zeeman interactions. Experimental values of relevant parameters, including the magnetic field of 0.4 mT, are assumed. We construct the total scattering wave function in a complete basis set containing electronic spin, nuclear spin and rotational angular momenta.

We solve the coupled-channels equations using a renormalized Numerov propagator with step-size doubling. The wave-function ratios are propagated to large interatomic separations, transformed to the diagonal basis, and the K and S matrices are extracted by imposing the long-range scattering boundary conditions in terms of Bessel functions. As an entrance channel, we assume Yb^+ in the $|F=1,m_F=-1\rangle$ state and Li in the $|F=1/2,m_F=-1/2\rangle$ or $|F=1/2,m_F=1/2\rangle$ state, while all other allowed channels are included in the model. The inelastic rate constants and scattering lengths are obtained from the elements of the S matrix summed over relevant channels including different partial waves l.

We calculate the rate constant for spin-changing collisions $K(E,a_S,a_T)$ as a function of the singlet and triplet scattering lengths. The scattering lengths of the singlet and triplet potentials are fixed by applying uniform scaling factors λ_i to the interaction potentials: $V_i(r)\rightarrow\lambda_iV_i(r)$. We express scattering lengths in units of the characteristic length scale for the atom–ion interaction $R_4=\sqrt{\mu C_4/\hbar}$. Next, the rate constant is convoluted with the ion's energy distribution induced by a controlled micromotion added to a thermal energy offset of $E_0/k_B=20$ μK.

$$\bar{K}(\bar{E},a_S,a_T)=\int_{E_0}^{E_0+\bar{E}_{eMM}}P_{\bar{E}_{eMM}}(E-E_0)K(E,a_S,a_T)dE \quad (10)$$

The probability of detecting the ion spin in $|F=0,m_F=0\rangle$ after preparing it in $|F=1,m_F=-1\rangle$ is calculated as

$$S(\bar{E},a_S,a_T,n_L)=1-\exp(-n_L\bar{K}(\bar{E},a_S,a_T)/K_L) \quad (11)$$

where n_L is the number of Langevin collisions and $K_L=2\pi\sqrt{C_4/\mu}$ is the Langevin collision rate coefficient. The singlet and triplet scattering lengths are found together with the number of Langevin collisions by minimizing the χ^2 function

$$\chi^2(a_S,a_T,n_L)=\sum_{i=1}^{N_{exp}}\left(\frac{S_{exp}(\bar{E}_i)-S(\bar{E}_i,a_S,a_T,n_L)}{\sigma_i}\right)^2 \quad (12)$$

which quantifies how well our theoretical model reproduces the measured probabilities $S_{exp}(\bar{E}_i)$. Here, N_{exp} denotes the number of datapoints and σ_i their experimental error. The numerical minimization of χ^2 yields $a_S=1.2(\pm0.3)R_4$, $a_T=-1.5(\pm0.7)R_4$ and $n_L=1.2(\pm0.4)$, where the uncertainties of the theoretical values are obtained by imposing that χ^2 gives a P value equal to or better than 0.05. Extended Data Fig. 4 shows corresponding χ^2 dependence on the scattering lengths.

Data availability

The data that support the plots within this paper and other findings of this study are available from the corresponding author upon reasonable request. Source data for Figs. 2 and 3 and Extended Data Figs. 1–4 are provided with the paper.

References

31. Joger, J. et al. Observation of collisions between cold Li atoms and Y^+ ions. *Phys. Rev. A* **96**, 030703(R) (2017).
32. Fürst, H. A. *Trapped Ions in A Bath of Ultracold Atoms*. PhD thesis, Univ. Amsterdam (2019).
33. Ewald, N. V., Feldker, T., Hirzler, H., Fürst, H. & Gerritsma, R. Observation of interactions between trapped ions and ultracold Rydberg atoms. *Phys. Rev. Lett.* **122**, 253401 (2019).
34. Taylor, P. et al. Investigation of the $^2S_{1/2}-^2D_{5/2}$ clock transition in a single ytterbium ion. *Phys. Rev. A* **56**, 2699–2704 (1997).

Acknowledgements

This work was supported by the European Union via the European Research Council (Starting Grant 337638) and the Netherlands Organization for Scientific Research

(Vidi Grant 680-47-538, Start-up Grant 740.018.008 and Vrije Programma 680.92.18.05) (R.G.). D.W. and M.T. were supported by the National Science Centre Poland (Opus Grant 2016/23/B/ST4/03231) and PL-Grid Infrastructure. We thank J. Walraven and C. Coulais for comments on the manuscript.

Author contributions

T.F. and R.G. conceived the experiment. T.F., H.F., H.H., N.V.E. and M.M. performed the experiment. H.F. and R.G. performed molecular dynamics simulations, D.W. and M.T. performed quantum scattering simulations. All authors contributed to discussions about the experiment, the analysis of the data and the preparation of the manuscript.

Competing interests

The authors declare no competing interests.

Additional information

Extended data is available for this paper at https://doi.org/10.1038/s41567-019-0772-5.

Supplementary information is available for this paper at https://doi.org/10.1038/s41567-019-0772-5.

Correspondence and requests for materials should be addressed to R.G.

Reprints and permissions information is available at www.nature.com/reprints.

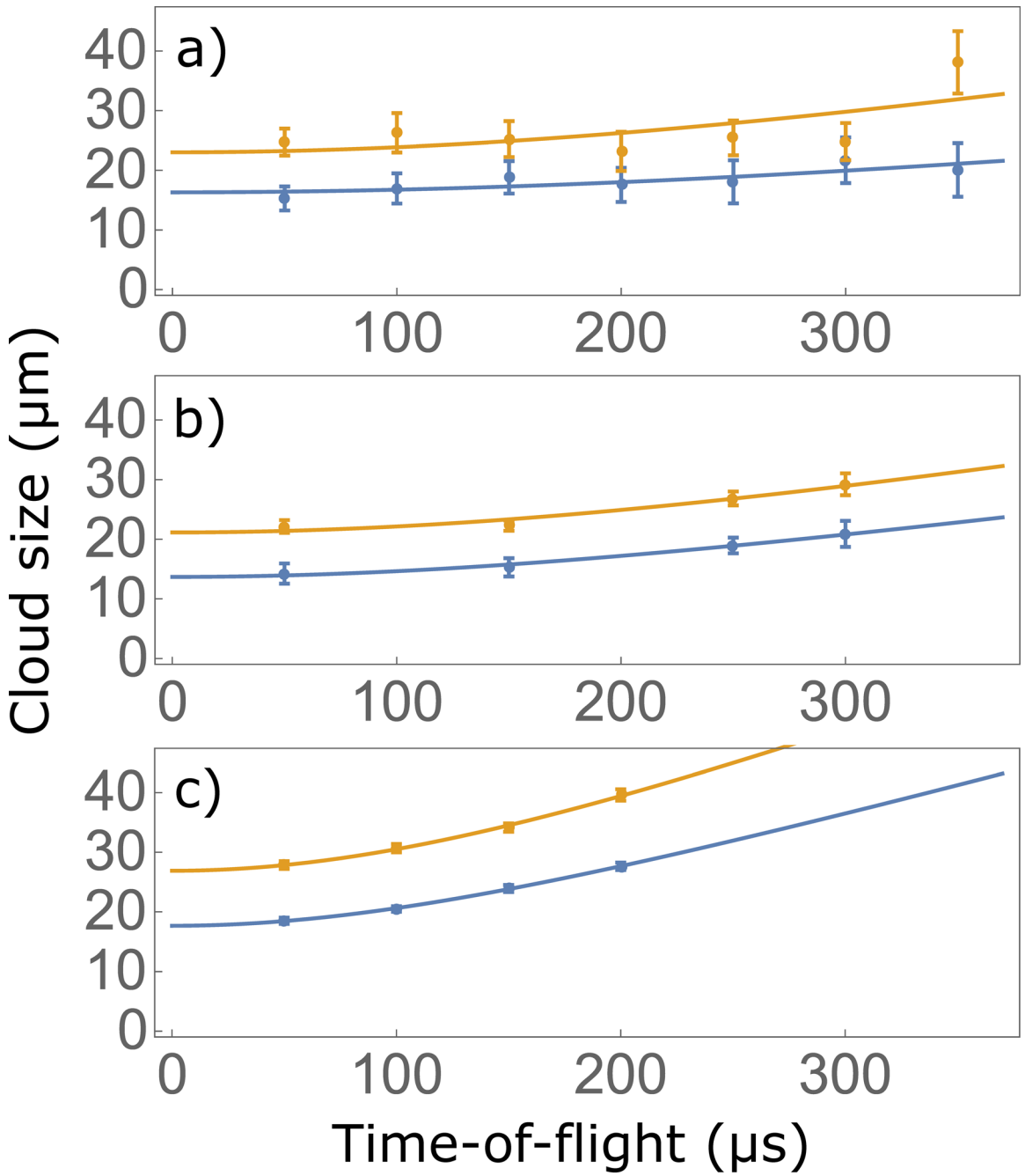

Extended Data Fig. 1 | Time-of-flight (TOF) data of the atomic cloud after release from the dipole trap. We plot σ_x (blue) and σ_y (yellow). We average the temperature T_x and T_y to determine the atom temperature T_a **a**, TOF data for cold atoms after a buffer gas cooling time of 1 s. We determine an average atom temperature of $T_a = 2.0(0.8)$ μK. The error bars are quite large for this measurement as the atomic density is at the lower limit of what we can reliably measure in our system. **b**, TOF data for cold atoms before the buffer gas cooling. We determine $T_a = 2.6(0.3)$ μK. **c**, TOF data for the atomic cloud used for the spin-exchange rate measurement, we determine a temperature of $T_a = 11.6(0.5)$ μK. Error bars denote standard deviations of fitted cloud sizes.

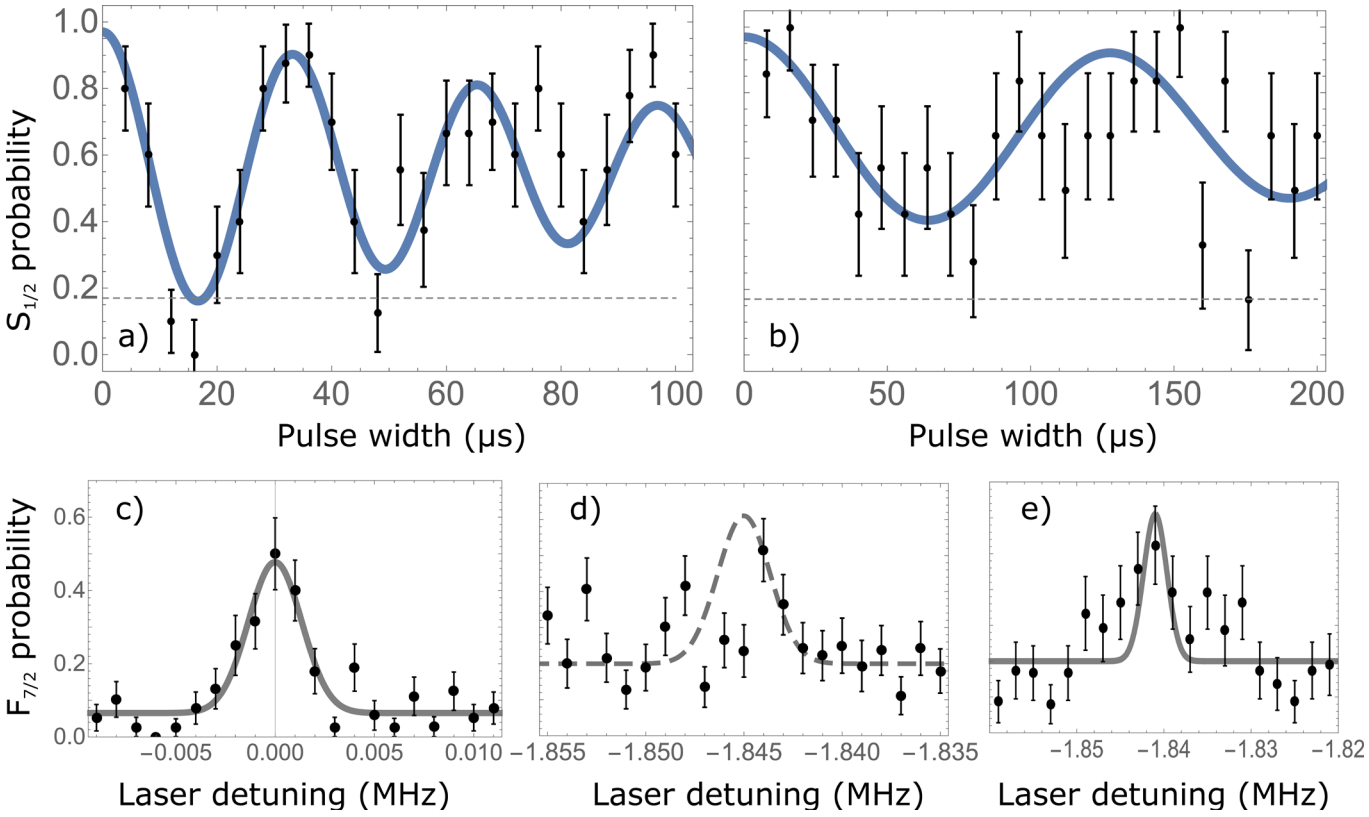

Extended Data Fig. 2 | Micromotion analysis with resolved sideband spectroscopy. In part **a** and **b** Rabi oscillations on the carrier and the micromotion sideband for optimal compensation settings are plotted. From a comparison of the Rabi frequencies $\Omega_{car} = 2\pi \times 32.0(0.8)$kHz and $\Omega_{MM} = 2\pi \times 7.0(0.5)$ kHz in combination with the applied laser powers of $P_{411} = 32$μW and $P_{411} = 840$μK, respectively we obtain a residual micromotion energy of $\bar{E}_{eMM}/k_B = 21.5(1.5)$μK. Part c shows a frequency scan over the carrier transition, carried out with a laser power of $P_{411} = 61$μW. A clear peak is visible. For the data plotted in part **d** the frequency of the laser is shifted by $-\Omega_{rf} = -1.85$MHz compared to **c** and the power is increased to $P_{411} = 21.7$mW. At the expected resonance frequency for the micromotion sideband we do not see a clear peak, only the background is higher compared to **c** due to off-resonant carrier excitation at these high laser powers. If we shift the ion out of the optimal position for minimal micromotion we observe a clear resonance again as plotted in **e**. We conclude that the Rabi frequency Ω_{MM} on the micromotion sideband presented in **e** is not larger than the Rabi frequency on the carrier Ω_{car} presented in **c**. From this we obtain an upper limit of the axial micromotion at the optimal position of $\bar{E}_{eMM}/k_B = 33$μK. Error bars correspond to quantum projection noise.

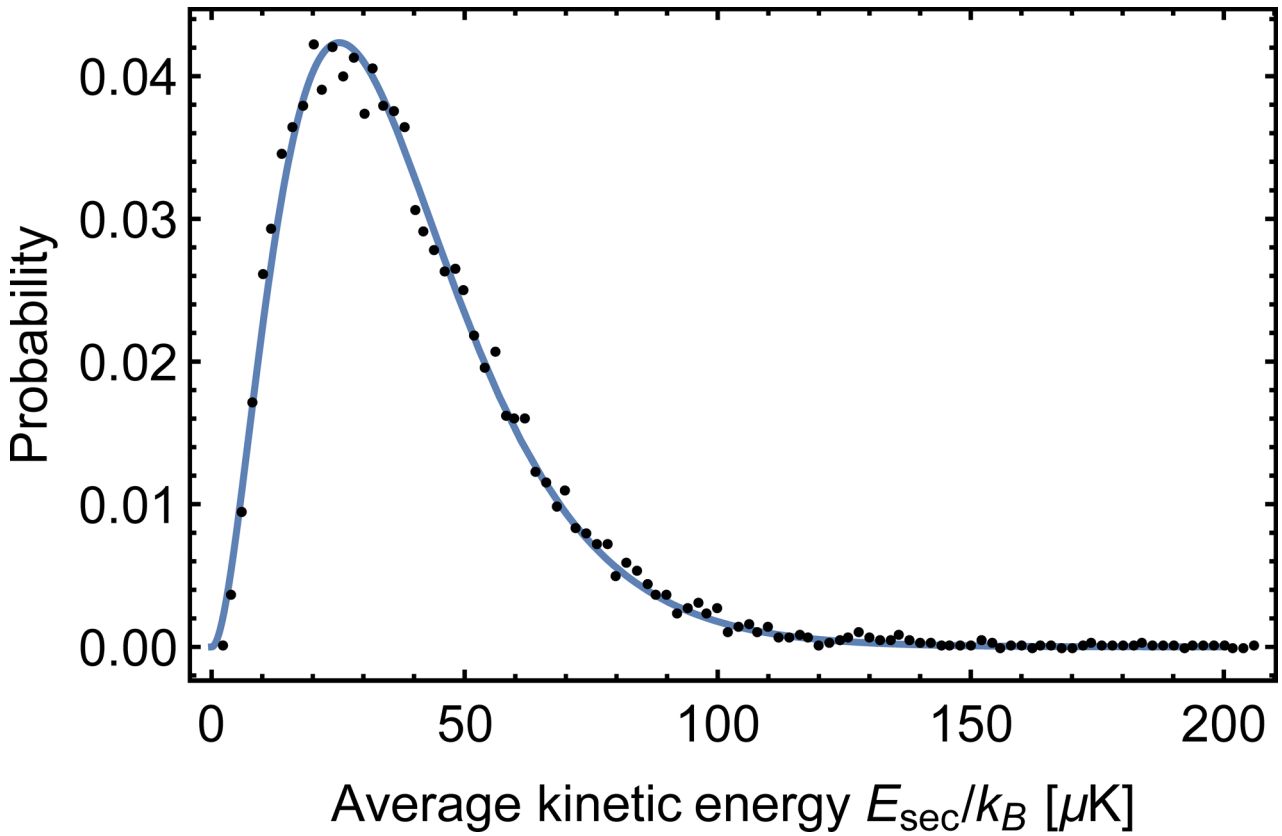

Extended Data Fig. 3 | Calculated energy distribution after buffer gas cooling of the ion using the parameters from the experiment. The frequency of average secular kinetic energies is shown and fitted with a thermal distribution for a harmonic oscillator with a temperature of $T^{\perp}_{sec} = 38.2\,\mu K$. No observable deviation from the thermal distribution is found. The results shown are from 300 simulation runs. In these simulations, the secular kinetic energy of the ion was obtained by filtering out energy contributions with a frequency higher than half the trap drive frequency, $\Omega_{rf}/2$, as explained in ref. [26].

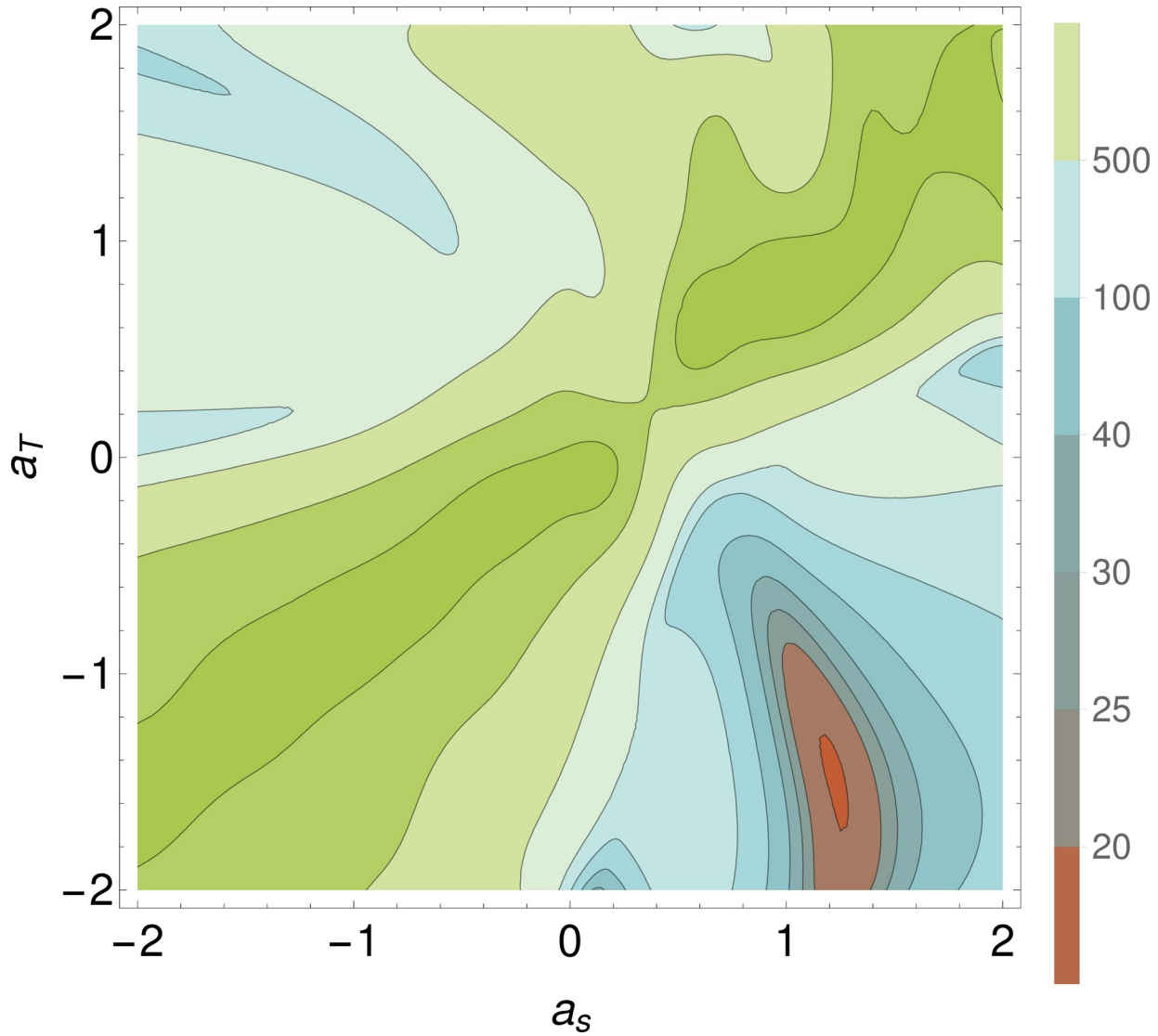

Extended Data Fig. 4 | χ^2 as a function of the singlet a_S and triplet a_T scattering lengths with the number of Langevin collisions optimized for each set of scattering lengths.